Ore Geology Reviews 73 (2016) 1–12

Contents lists available at ScienceDirect

Ore Geology Reviews

journal homepage: www.elsevier.com/locate/oregeorev

Identifying geochemical anomalies associated with Sb–Au–Pb–Zn–Ag mineralization in North Himalaya, southern Tibet

Xiang Sun [a,*], Youye Zheng [a,b], Changming Wang [a], Zhongying Zhao [c], Xuebin Geng [a]

[a] State Key Laboratory of Geological Processes and Mineral Resources, China University of Geosciences, Beijing 100083, China
[b] Institute of Geological Survey, China University of Geosciences, Wuhan 430074, China
[c] Petrochina Research Institute of Petroleum Exploration & Development, Beijing 100083, China

ARTICLE INFO

Article history:
Received 23 August 2015
Received in revised form 13 October 2015
Accepted 14 October 2015
Available online 22 October 2015

Keywords:
Statistical method
Fractal
Singularity
Targeting

ABSTRACT

The North Himalaya is a prospective area for Sb, Sb–Au, Au, Pb–Zn(−Ag), and Sb–Pb–Zn–Ag mineralization. Geochemical anomalies for mineralizing elements and element associations were identified using concentration–area (C–A) fractal model together with statistical analyses, including the mean ± 2 standard deviation (Mean + 2STD) and the median ± 2 median absolute deviation (Median + 2MAD). The results show that the Mean + 2STD for log-transformed data and C–A model could well identify the geochemical anomalies associated with mineralization in the North Himalaya. Sb + Au anomalies show a better spatial association with Sb, Sb–Au, and Sb–Pb–Zn–Ag deposits than those of single Sb element. Au anomalies are associated with all deposits, and Pb + Zn + Ag anomalies are associated with Pb–Zn and Sb–Pb–Zn–Ag deposits. In addition, weak anomalies associated with Sb mineralization can be identified by the singularity method. With the utilization of the Sb + Au, Sb, Au and Pb + Zn + Ag anomalies identified by C–A fractal model and Mean + 2STD for log-transformed data, as well as the singularity method, we can facilitate the exploration targeting of various deposits in the North Himalaya. In addition, our results also show that principal component analysis (PCA) of centered logratio (clr) transformed data can accurately recognize three different geochemical assemblage compositions representing three different types of mineralization (i.e., Au, Pb–Zn–Ag and Sb) in the North Himalaya.

1. Introduction

Stream sediment surveys play an important role in mineral resource exploration, and different types of deposits have been discovered in China (Xie et al., 1997, 2008). However, it is challenging to process such data to detect multivariate geochemical patterns and signals associated with mineralization (Carranza, 2004). Principal component analysis (PCA) is an important tool in data analysis that can reduce the dimension of variables or identify factors that detect hidden structures in multivariate data (Cheng et al., 2006; Reimann et al., 2008). Several varieties of PCA, in addition to classic PCA, can be found in the literature, including fuzzy masking PCA (FMPCA; Cheng et al., 2011) and robust PCA (RPCA; Zuo, 2014). These approaches can be applied to (1) raw data, (2) log-transformed data, (3) additive logratio (alr) transformed and centered logratio (clr) transformed data (Aitchison, 1986), and (4) isometric logratio (ilr) transformed data (Egozcue et al., 2003). Carranza (2010) applied classic PCA to log-transformed stream sediment geochemical data and derived a new factor for Cu–Ni–As, represented by the integrated third principle component (PC3) with positive loadings of Cu and As × (means multiply) fourth principle component (PC4) with positive loadings of Ni and As, as a proxy for Au mineralization in the Aroroy district in Philippines. Using this method, anomalous areas were found to exhibit good spatial associations with known epithermal Au deposits. Zheng et al. (2014a) conducted PCA on raw data and used PC4 with positive loadings of Cu and Au to reveal geochemical anomalies at Zhunuo in the Gangdese belt, southern Tibet, and this played a role in the discovery of the Zhunuo porphyry Cu deposit. Based on RPCA on geochemical data from the Fanshan district, China, Zuo (2014) considered that first principle component (PC1) comprises two different compositional groups: (1) Pb, Zn, Sn, W, Mo, Bi, Hg, and Ag with positive loadings that characterize epithermal-type Cu–Au mineralization; and (2) As, Au, Cu, Sb, and Mn with negative loadings that characterize epithermal-type Cu–Au mineralization. Subsequently, spectrum–area (S–A) fractal modeling was applied to decompose the mixed geochemical patterns, from which a number of geochemical anomalies were identified.

Several methods have been proposed to separate geochemical anomalies from background, including (1) traditional statistical analysis techniques such as probability graphs (Sinclair, 1974), univariate and multivariate analysis methods (Tukey, 1977; Aitchison, 1986; Sun et al., 2009), and fractal and multifractal models such as number–size (N–S; Mandelbrot, 1983; Agterberg, 1995; Wang et al., 2010a, 2010b; Yang et al., 2015), concentration–area (C–A; Cheng et al., 1994; Deng

* Corresponding author.
E-mail address: sunxiang8003@sina.com (X. Sun).

http://dx.doi.org/10.1016/j.oregeorev.2015.10.020
0169-1368/

et al., 2009, 2010, 2011; Wang et al., 2011a, 2012), concentration–distance (C–D; Li et al., 2003), concentration–volume (C–V; Afzal et al., 2011), spectrum–area (S–A; Cheng et al., 2000), and the local singularity (Cheng, 2007). Reimann et al. (2005) compared various statistical methods for the determination of element concentration threshold values and showed that boxplot, median ± 2 median absolute deviations (Median + 2MAD) and empirical cumulative distribution functions are better suited for estimating anomaly threshold values than is the mean ± 2 standard deviations (Mean + 2STD). Considering the spatial autocorrelation nature of the geochemical data, fractal and multifractal methods have been widely applied to identify geochemical anomalies (e.g., Cheng, 2007; Sun et al., 2010a; Zuo et al., 2013).

Many Sb, Sb–Au, Au, Pb–Zn, and Sb–Pb–Zn–Ag deposits occur throughout North Himalaya, southern Tibet, China. Hou and Cook (2009) commented on the Sb, Sb–Au, and Au deposits but did not discuss a genetic model for the mineralization. Nevertheless, they did suggest that the mineralization in the region was related to the South Tibet Detachment System (STDS) and probably formed during the Miocene in a post-collisional setting. However, Sun et al. (2010b) and Zhai et al. (2014) suggested the Bangbu Au and Mazhala Sb–Au deposits to be orogenic-type based on the fluid inclusion studies. Recent researches have shown that the mineralization at Zhaxikang formed during two distinct phases: an early phase of Pb–Zn(−Ag) mineralization and a later Sb mineralization (Zheng et al., 2012, 2014b; Liang et al., 2013). The multiple phases and various types of mineralization in the North Himalaya suggest that the concentration distributions of elements associated with mineralization are complicated.

The objective of this paper is to apply various traditional statistical and fractal methods to stream sediment geochemical data collected in the North Himalaya, southern Tibet, and evaluate the best approaches for characterizing anomalies associated with particular styles of mineralization. Our results will be helpful for not only understanding the mineralization in the North Himalaya but also the exploration targeting.

2. Regional geology in the north Himalaya

As one of the world's largest and youngest collisional orogens, the Himalaya can be divided into four belts (from north to south): North Himalaya, Higher Himalaya, Lower Himalaya, and sub-Himalaya (Fig. 1A). These belts are separated (from north to south) by the South Tibet Detachment System (STDS), the Main Central Thrust (MCT), and the Main Boundary Thrust (MBT), respectively, and are flanked to the south by the Main Frontal Thrust (MFT) (Yin, 2006). The North Himalaya is composed of the Tethyan Himalayan sequence (THS), which consists predominantly of low-grade Proterozoic to Cretaceous metasediments that are thought to have been deposited along the northern edge of the Indian continent (Liu and Einsele, 1994; Pan et al., 2004; Fig. 1B). The THS was generally divided into the northern and southern zones (Liu and Einsele, 1994), separated by the north-dipping Gyrong–Kangmar thrust (GKT in Fig. 1A; the term is a synonym to Gyrong–Tingri–Gamba–Luozha fault, Pan et al., 2004). It should be noted that ore deposits discovered up to now in the southern Tibet are located in the northern zone.

Igneous rocks in the North Himalaya are dominated by the Late Jurassic–Early Cretaceous mafic rocks and Cenozoic granitoids. The Late Jurassic–Early Cretaceous (145–130 Ma) mafic rocks are exposed in the Jurassic–Cretaceous sedimentary sequences and consist of basaltic lavas, mafic sills and dikes, and gabbroic intrusions, the petrogenesis of which were suggested to be associated with the mantle plume (Zhu et al., 2008, 2009). The Cenozoic granitoids in the North Himalaya consist of the Eocene granitoids and the Miocene leucogranites, two-mica

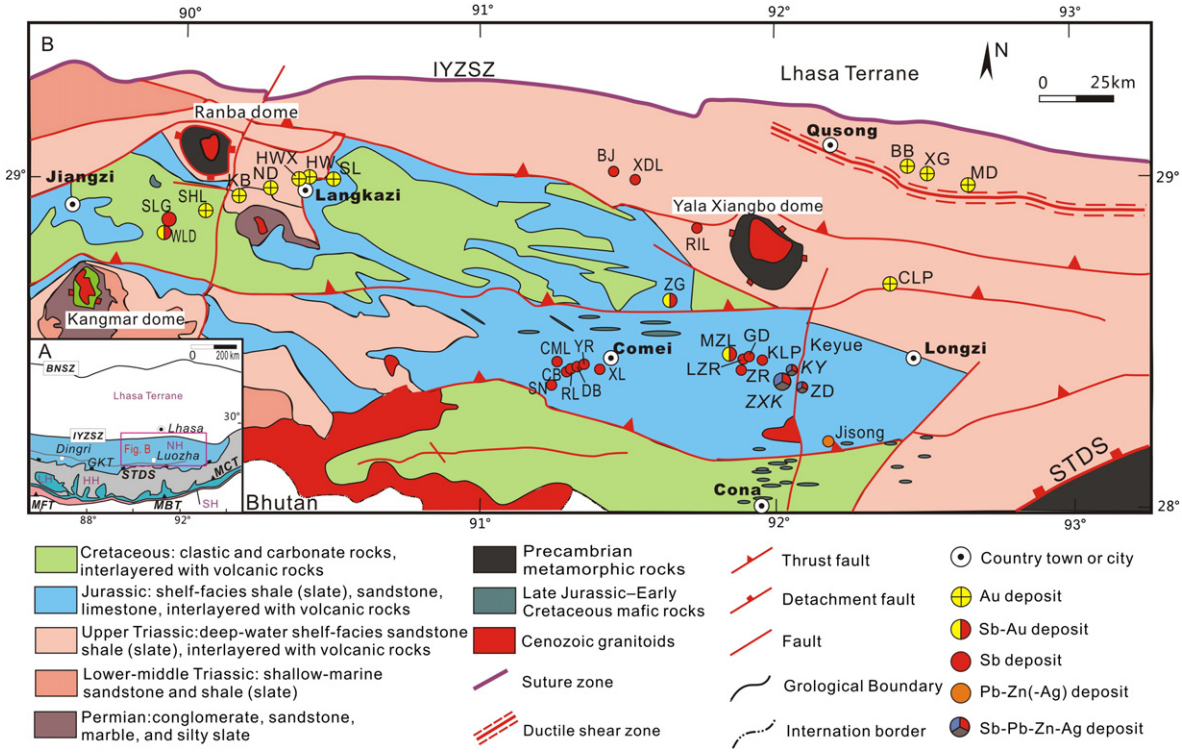

Fig. 1. (A) Tectonic outline of the Tibetan Plateau (after Yin, 2006). (B) Geological map of the North Himalayan Polymetallic Metallogenic Belt (modified after Zhu et al., 2011; Zheng et al., 2014b). BNSZ, Bangong–Nujiang Suture Zone; IYZSZ = Indus–Yarlung Zangbo Suture Zone, MFT = Main Frontal Thrust, MBT = Main Boundary Thrust Fault, MCT = Main Central Thrust Fault, STDS = South Tibet Detachment System, NH = North Himalaya, HH = Higher Himalaya, LH = Lower Himalaya, SH = Sub-Himalaya. Au deposits: XG–Xigong, BB–Bangbu, MD–Muda, CLP–Chalapu, HW–Hawong, HWX–Hawongxi, KB–Kangbugunba, SL–Sheli, ND–Naodong, and SHL–Shengla. Sb deposits: GD–Guidui, LZR–Longzhongri, KLP–Kelupu, ZR–Zheri, CB–Cheqiongzhuobu, YR–Yongri, RL–Rangla, XL–Xuela, DB–Duoba, CML–Chimalong, SN–Shangni, SLG–Shalagang, BJ–Baijia, RIL–Rila, and XDL–Xiangdala. Sb–Au deposits: MZL–Mazhala, ZG–Zhegu, and WLD–Wuladui. Pb–Zn(−Ag) deposit: JS–Jisong. Sb–Pb–Zn–Ag deposits: ZXK–Zhaxikang, KY–Keyue, and ZD–Zhedang.

granites, and diorite. Recently reported Eocene granitoids are restricted to the Yala Xiangbo dome, including (1) the weakly deformed ~44 Ma Dala two-mica granite, (2) the intensely deformed ~42 Ma Yala Xiangbo two-mica granite, and (3) the undeformed ~35 Ma granite sheets and dikes usually cross-cutting the two-mica granite and occurring along normal or detachment faults around the Yala Xiangbo dome (Zeng et al., 2011; Aikman et al., 2008, 2012; Hou et al., 2012). Since the collision between India with Asia at 65–60 Ma (Ji et al., 2009; Zhu et al., 2011; Wu et al., 2014), the North Himalaya has experienced tectonic compression, represented by E–W striking thrust faults and associated folding, and subsequent extension represented by N–S trending rifts, the development of the STDS, and the unroofing of gneiss domes (Armijo et al., 1986; Taylor et al., 2003; Zhang et al., 2012).

3. Regional metallogenesis and typical ore deposits in the North Himalaya

Many hydrothermal Au, Sb, Sb–Au, Pb–Zn and Sb–Pb–Zn–Ag deposits have been found in the North Himalaya (Fig. 1B). Au deposits (e.g., Bangbu, Chalapu, and Haweng) are predominantly hosted in the Triassic metasedimentary rocks. Sb deposits (e.g., Kelupu, Cheqiongzhuobu, and Shalagang) are mainly hosted in the Jurassic and Cretaceous metasedimentary rocks and to a lesser extent in the Triassic metasedimentary rocks. Both Sb–Au (e.g., Mazhala, Zhegu, and Wuladui) and Pb–Zn deposits (i.e., Jisong) are hosted in the Jurassic metasedimentary rocks. However, the Sb–Au mineral systems occur near the Sb ones, whereas the Pb–Zn deposits are located more than 35 km from the Sb ores. The Sb–Pb–Zn–Ag deposits are hosted in the Jurassic metasedimentary rocks, including Zhaxikang, Keyue, and Zedang. The Late Jurassic–Early Cretaceous mafic rocks in most of these deposits exhibit alteration and host Au, Sb, and Sb–Au mineralization. Generally, Au and Sb–Au orebodies trend nearly east–west, whereas Sb and Sb–Pb–Zn–Ag orebodies trend nearly north–south. Three different types of typical deposits are introduced below.

3.1. Zhaxikang Sb–Pb–Zn–Ag

The Zhaxikang Sb–Pb–Zn–Ag deposit is located to west of Longzi city. To September 2012, it has proven and probable reserves of 18 Mt. at 0.6 wt.% Sb, 2.0 wt.% Pb, 3.5 wt.% Zn, and 78 g/t Ag (HMCL, 2012). The ore district is underlain by the Early–Middle Jurassic Ridang Formation, which can be divided into three parts. From bottom to top, these are coarse-grained metasandstone intercalated with slate, slate intercalated with medium to fine-grained metasandstone, and dark-gray carbonaceous slate intercalated with fine-grained metasandstone and marly limestones (Fig. 2). Early Cretaceous diabase (a zircon U–Pb age of 133.4 ± 2.2 Ma; Zheng et al., 2014b) and rhyolite (a zircon U–Pb age of 135.33 ± 0.62 Ma; Lin et al., 2014) crop out south of the Zhaxikang deposit. Several N–S- and NE-trending strike-slip extensional faults crosscut the Ridang Formation, many of which host vein-type ores. Three different styles of mineralization occur within the Zhaxikang deposit including Pb–Zn–Ag, Sb, and Sb–Pb–Zn–Ag veins, among which the Sb–Pb–Zn–Ag veins are the most important veins. The mineralization at Zhaxikang was suggested to form during two separate pulses. The early pulse produced Pb–Zn–Ag veins composed mainly of Mn–Fe carbonate + sphalerite + galena, whereas the later pulse produced veins comprising quartz + stibnite and quartz + calcite + sphalerite + galena + Sb–Pb(−Ag) sulfosalt (Zheng et al., 2012). Overprinting of the Pb–Zn–Ag veins by later Sb-rich fluids led to the deposition of stibnite and a range of Sb–Pb sulfosalt minerals at the expense of the primary galena and sphalerite.

3.2. Chalapu Au

The Chalapu Au deposit is located to northeast of Longzi city and has a resource of 14.3 t gold metal at a grade of 3.9 g/t to 2005. The strata in the ore district are characterized by the sandy slate and carbonaceous slate of the Late Triassic Nieru Formation (Fig. 3). They were intruded by the diabase and diorite. Gold-bearing veins developed along either the fractured zones within the rocks of the Nieru Formation or along the contacts between the diabase and the rocks of the Nieru Formation. The ore minerals are predominantly composed of pyrite and arsenopyrite, with minor amounts of stibnite and trace amounts of sphalerite, galena, chalcopyrite, and native gold. The gangue minerals are quartz, calcite, white mica, sericite, chlorite and illite. The styles of gold mineralization include the disseminated, vein-type, and breccia-type ores, which are similar to those in the Jiaodong and Sanjiang districts (Deng et al., 2011, 2014a, 2014b, 2015).

3.3. Cheqiongzhuobu Sb

The Cheqiongzhuobu Sb is located in the Cuomei area and has a resource (determined in 2003) of 16.5 t Sb metal at a grade of 3.7%. The rocks in the ore district include the slate intercalated with metasiltstone of the Late Jurassic Weimei Formation, dacite, andesite, and slate intercalated with metasiltstone of the Middle Jurassic Zhela Formation, and slate intercalated with metasandstone and limestone of the Early-Middle Jurassic Ridang Formation (Fig. 4). The aplite and diabase intruded into the Ridang Formation. A N–S-trending extensional fault crosscuts the Ridang Formation and hosts antimony orebodies. The ore minerals in the veins are stibnite, pyrite, and arsenopyrite. The gangue minerals are quartz and calcite. The styles of mineralization at Cheqiongzhuobu include the quartz vein-type, calcite vein-type and breccia-type ores.

4. Stream sediment geochemical data

The stream sediment geochemical data used in this paper include geochemical concentrations of six ore-forming elements (numbers in parentheses denote detection limits in ppm), i.e., Au (0.0003), As (1), Sb (0.1), Pb (2), Zn (10), and Ag (0.02). A total of 8055 stream sediment samples were collected at a density of approximately one sample per 7 km^2 within the area 89°15′–93°15′N, 28°–29°15′E. The concentration of Au was determined by graphite furnace–atomic absorption spectrometry (GF–AAS), Sb by hydride generation–atomic fluorescence spectrometry (HG–AFS), Pb by inductively coupled plasma–mass spectrometry (ICP–MS), and Zn by inductively coupled plasma–atomic emission spectrometry (ICP–AES). For more details on the sampling and analysis procedures, see Xie et al. (1997, 2008) and Wang et al. (2011b).

Raw data of element concentrations are all significantly positively skewed (Table 1). Log-transformation alleviates skewness in the data and the element concentrations show moderately symmetric distributions (Fig. 5A–C). Q–Q plots also show that some element (e.g., Au, Sb, Pb) concentrations do not follow log-normal distributions (Fig. 5D–F). Therefore, both raw data and log-transformed data of element concentrations are not normally distributed.

5. Methods

The analyses employed the following geochemical processing methods that are used routinely to delineate anomalies.

5.1. Principal component analysis (PCA)

To unravel the multi-element associations describing the different mineralization in the North Himalaya, we performed PCA. To address the closure problem in multivariate statistical analysis of compositional datasets, we applied a centered logratio (clr) transformation (Aitchison, 1986) to the elemental data prior to PCA. We applied the Kaiser (1960) criterion to extract only principal components (PCs) with eigenvalues greater than 1, meaning only PCs that explain as much variability

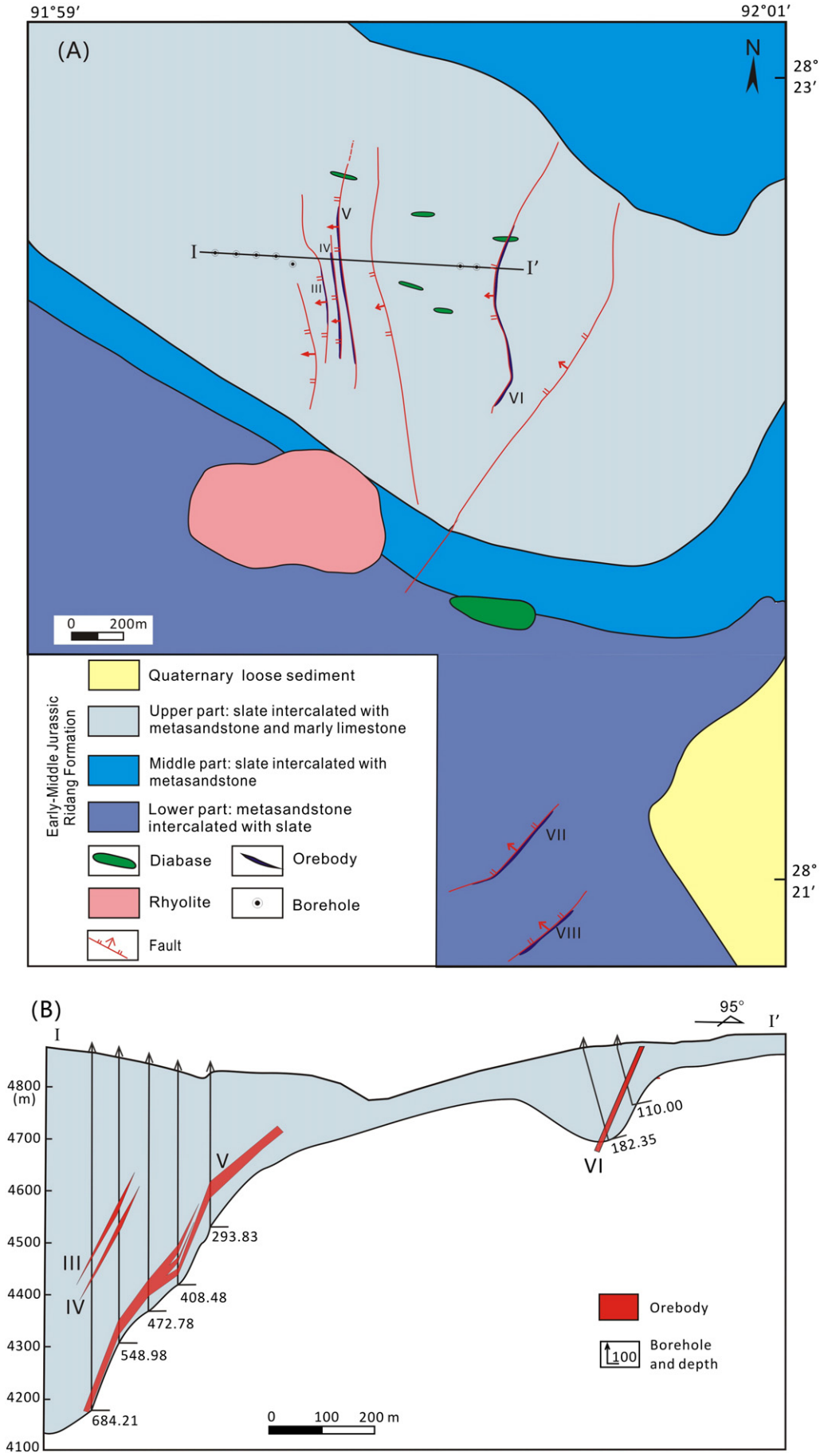

Fig. 2. (A) Geological map of the Zhaxikang Sb–Pb–Zn–Ag deposit. (B) Cross-section along line I–I′ indicated in Fig. 2A.

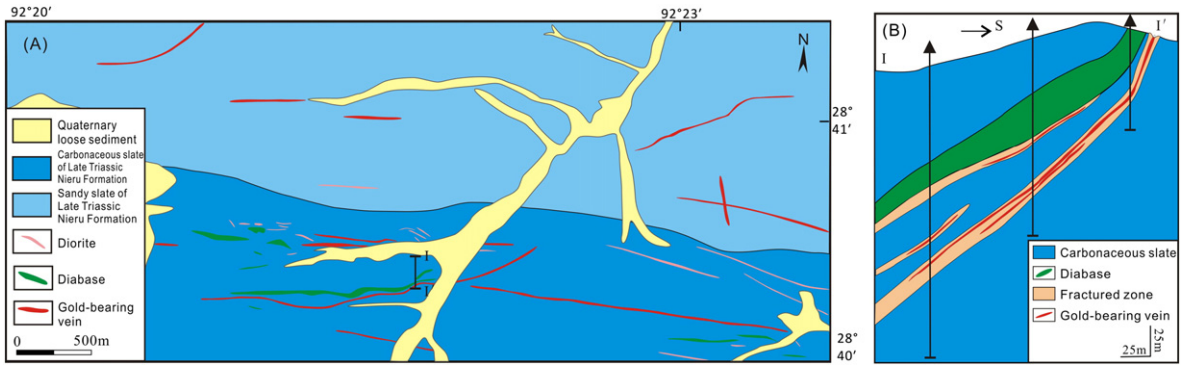

Fig. 3. (A) Geological map of the Chalapu Au deposit. (B) Cross-section along line I–I′ indicated in Fig. 3A.

equivalent at least one original variable are considered important. The extracted PCs were subjected to orthogonal rotation by the Varimax method (Kaiser, 1960) to maximize the variability (i.e. to strongly differentiate) among all input variables and, thus, facilitate interpretation of the factor loadings.

5.2. Mean + 2 standard deviation (mean + 2STD) and median + 2 median absolute deviation (median + 2MAD)

The use of Mean + 2STD methods is applicable only to data with normal distribution. However, the geochemical data in the North Himalaya do not follow the normal distribution (Fig. 5). In this study, we firstly reject those extreme values (over Mean + 3STD or below Mean-3STD) from the raw data through multiple iterations until the remaining data follow the normal distribution, and then use the Mean + 2STD of the final processed data as the threshold values. In addition, the Median + 2MAD method is also applied to raw data and log-transformed data in order to compare these two methods. The MAD stands for Median absolute deviation while the STD stands for standard deviation (Tukey, 1977).

5.3. Concentration–Area (C–A) model

The C–A fractal model, originally developed by Cheng et al. (1994), is defined as.

$$A(r \geq r_i) = c r_i^{-D}, \quad (1)$$

where $A(r \geq r_i)$ represents the area enclosed by contours with concentration (r) greater than or equal to the contour value r_i, and D denotes the fractal dimension for the C–A fractal model. $A(r \geq r_i)$ and r_i follow a power-law relationship.

C–A plot describes straight lines on a log–log graph, on which single or multiple straight line segments can be recognized. A single line most likely represents the fractal distribution of the geochemical background, whereas two straight-line segments most likely represent the background together with an added geochemical population (i.e. mineralization). The concentration value of the cross points between the two segments represents the threshold value for an anomaly. In C–A plot comprising multiple straight-line segments, the concentration values of many cross points may represent several geochemical populations,

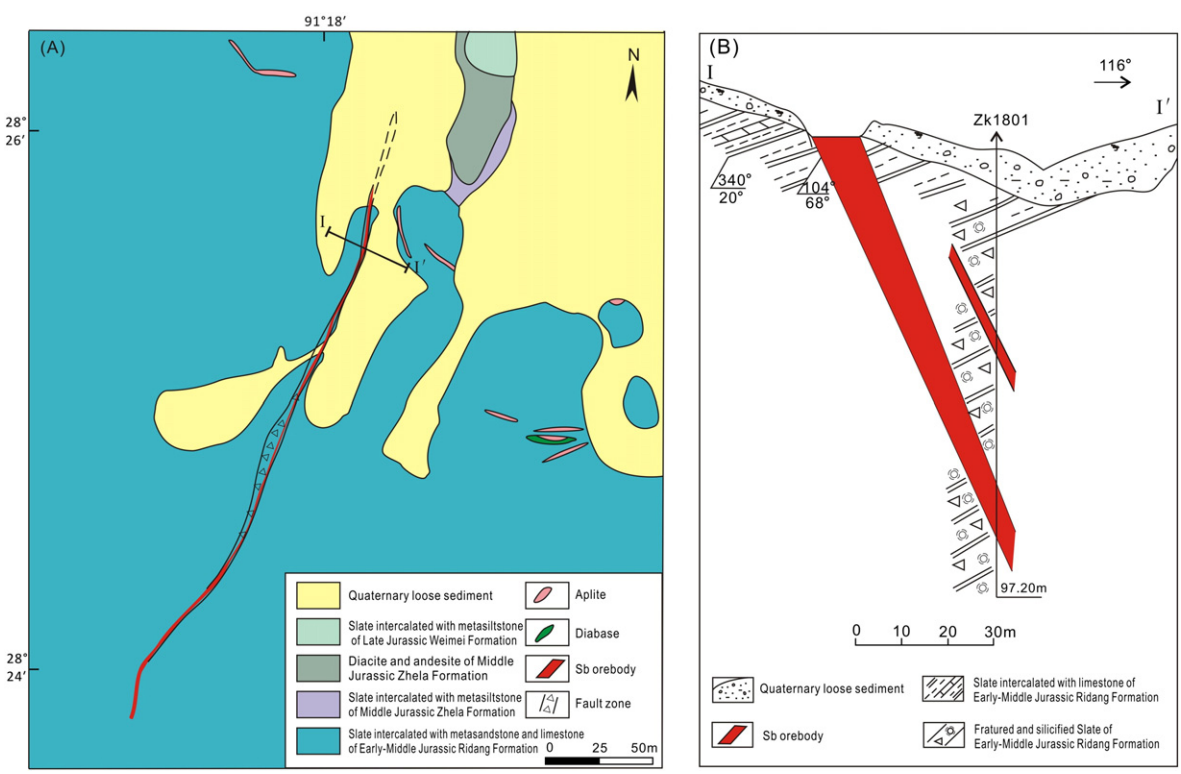

Fig. 4. (A) Geological map of the Cheqiongzhuobu Sb deposit. (B) Cross-section along line I–I′ indicated in Fig. 4A.

Table 1
Statistical parameters of the element concentrations in the stream sediment geochemical data from the North Himalaya.

Element	Au	As	Sb	Pb	Zn	Ag
Number of samples	8555	8555	8555	8555	8555	8555
Mean	2.86	31.44	2.09	30.16	88.28	97
STD	3.9	40.4	4.5	23.8	32.0	237.6
Median	2.01	20.44	1.06	26.70	84.84	72
Minimum	0.26	0.45	0.02	3.08	18.20	10
Maximum	137.9	1432	226.2	680.1	627	13,700
25th percentiles	1.40	13.09	0.68	22.73	72.30	60
75th percentiles	3.20	37.20	2.09	31.51	99.19	100
90th percentiles	5.10	63.63	3.98	39.22	115.17	130
95th percentiles	6.96	83.07	6.66	46.66	127.23	170
98th percentiles	9.79	124.30	11.25	67.49	151.41	270
Skewness	15.1	11.6	19.0	9.8	6.0	37
Kurtosis	382	281	736	139	76	1816

Note: The units for Au and Ag are ppb; the units for other elements are ppm. STD, standard deviation.

which may include a low background, high background, low anomaly, high anomaly, etc.

5.4. Local singularity method

The local singularity method is defined as the characterization of atypical behavior of physical processes that result in anomalous amounts of energy release, or material accumulation, within a narrow spatial–temporal interval. The singularity index can be estimated from element concentrations within small neighborhoods based on the following power-law distribution (Cheng, 2007):

$$\mu(\varepsilon) \propto \varepsilon^{\alpha}, \tag{2}$$

$$\mu(\varepsilon) \propto \rho \varepsilon^{d}, \tag{3}$$

$$\rho(\varepsilon) \propto \varepsilon^{\alpha - d}, \tag{4}$$

where $\mu(\varepsilon)$ and $\rho(\varepsilon)$ denotes the total amount and density of element concentrations, respectively; ε is a normalized distance measure, such as block cell edge; α is the singularity index; and d represents the Euclidean Dimension, which equals 2 when performing a 2D calculation. For a geochemical map, most of the areas are linked with a singularity value close to 2, which represents a normal distribution, whereas $\alpha > 2$ or $\alpha < 2$ represent enriched and depleted element concentrations, respectively (Cheng, 2007).

The window-based method (Cheng, 2007; Zuo et al., 2009; Sun et al., 2010a) is commonly used to calculate the singularity index α and, consequently, to delineate geochemical anomalies. This method involves the following steps: (1) define a set of sliding cells with variable sizes ($\varepsilon_1 < \varepsilon_2 < \ldots < \varepsilon_n$) at a given sampling point on a map, (2) calculate the total amount [$\mu_i(\varepsilon)$] or density [$\mu_i(\varepsilon)$] of element concentrations for each cell size, (3) plot $\log(\mu)$ against $\log(\varepsilon)$, or $\log(\rho)$ against $\log(\varepsilon)$, and (4) fit a straight line to the data using the least squares method. According to Eqs. (2) and (4) above, the α-value of the sampling point can be calculated from the slope of the straight line. The squared correlation coefficients can also be calculated to validate the linearity. The preceding analysis is repeated for all sampling points and the distribution of the singularity is mapped. Further details on the properties of singularities can be found in Cheng (2007) and Sun et al. (2010a).

6. Results

Two PCs were obtained through the PCA of the raw and clr-transformed stream sediment geochemical data (Table 2). The first

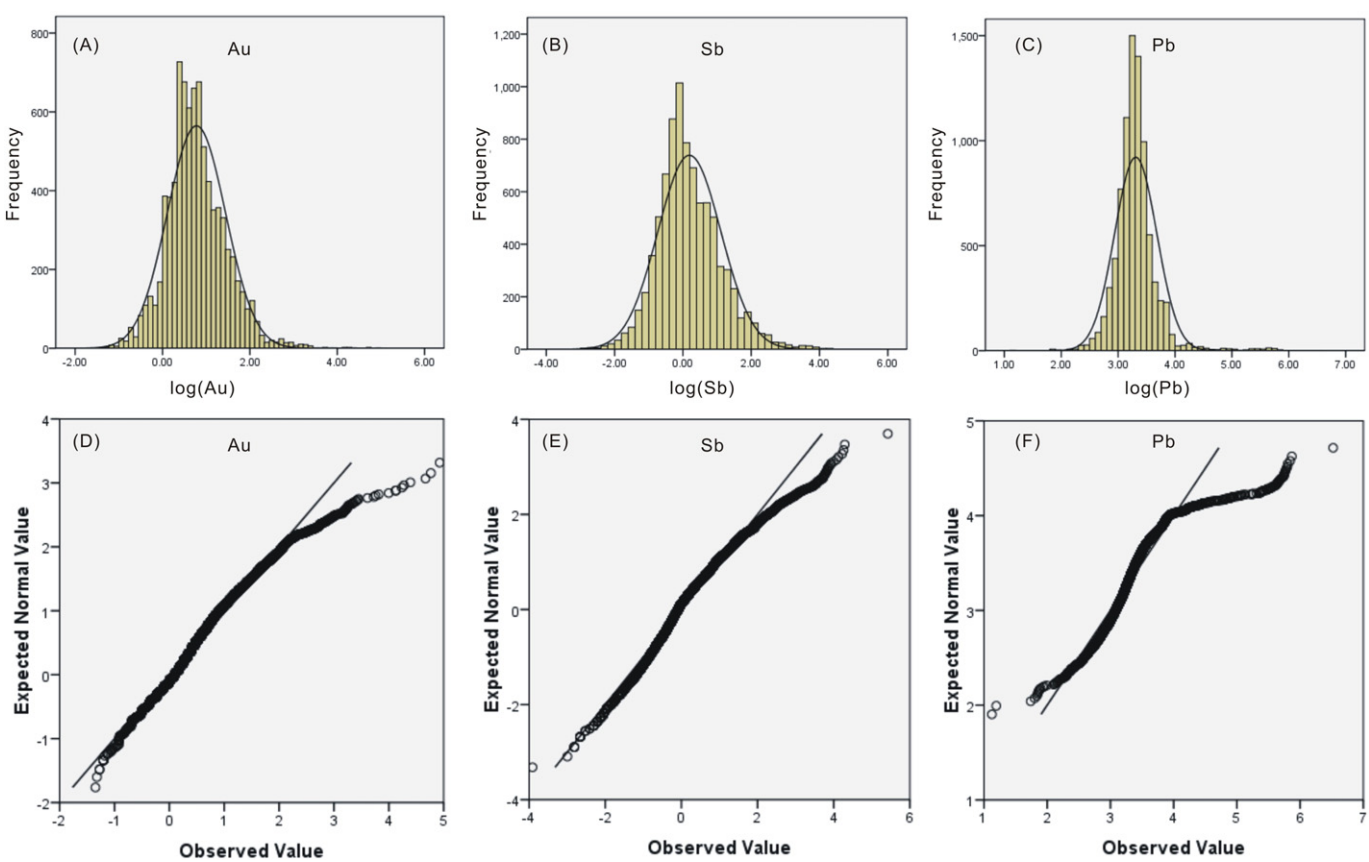

Fig. 5. Histograms of (A) Au, (B) Sb, and (C) Pb, and Q–Q plots of (D) Au, (E) Sb, and (F) Pb for the regional stream sediment geological data from the North Himalaya.

Table 2
Results of PC analysis of raw and clr-transformed geochemical data from the North Himalaya.

Component loading	Raw data		Clr-transformed data	
	PC1	PC2	PC1	PC2
Ag	0.74	0.03	0.80	0.09
As	0.13	0.82	0.33	0.75
Au	0.04	0.79	−0.11	0.80
Pb	0.82	0.00	0.76	0.11
Sb	0.63	0.29	0.46	0.65
Zn	0.66	0.09	0.67	0.16
Eigenvalues	2.07	1.39	2.00	1.67
% of variance	34.5	23.1	33.3	27.7
Cum. % of variance	34.5	57.6	33.3	61.0

Note: Clr denotes centered logratio (Aitchison, 1986).

Table 3
Anomaly threshold values, calculated using different methods, for stream-sediment data from the North Himalaya.

	Mean + 2STD		Median + 2MAD		C-A fractal model	
	Raw data	Log-transformed data	Raw data	Log-transformed data	Low anomaly	High anomaly
Au (ppb)	4.5	7.2	5.0	6.0	4.1	6.9
Sb (ppm)	2.6	6.4	3.9	4.3	4.0	29.4
Sb + Au	5.2	9.1	6.1	6.8	4.9	33.5
Au + As	5.0	7.6	5.2	6.0	4.0	6.5
Pb + Zn + Ag	4.4	4.7	4.9	7.8	5.2	24.4
Sb + Pb + Zn + Ag	6.9	8.4	8.3	7.9	11.8	46.9

Note: STD, standard deviation; MAD, median absolute deviation.

component (PC1) obtained from the raw data accounts for 34.5% of the total variances of the data and shows that all six elements provide positive contributions. The second component (PC2) obtained from the raw data accounts for 23.1% of the total variances and comprises two populations with positive loadings from Au, As and Sb, and with Pb, Zn, and Ag nearly equal to zero. The PC1–PC2 biplot (Fig. 6A) portrays the multi-element associations, namely: (1) Sb–Pb–Zn–Ag, probably describing mineralization at the Sb–Pb–Zn–Ag deposits (e.g., Zhaxikang), and (2) Au–As, probably describing mineralization at the Au deposits (e.g., Bangbu).

The PC1 and PC2 obtained from the clr-transformed data account for 33.3% and 27.7% of the total variances, respectively. PC1 is composed of positive loadings from Pb, Zn, Ag, Sb, and As, and negative loading from Au. PC2 is composed of positive loadings from all six elements. The PC1–PC2 biplot (Fig. 6B) portrays the multi-element associations, namely: (1) Pb–Zn–Ag, probably describing mineralization at the Pb–Zn(−Ag) deposits (e.g., Jisong), (2) Sb–As, probably describing mineralization at the Sb deposits (e.g., Rangla), and (3) Au, probably describing mineralization at the Au deposits.

To further delineate anomalies associated with Sb–Au mineralization (e.g., the Mazhala deposit) and compare anomalies of variables determined by different methods, the concentrations of Au and Sb, and the scores of element associations including Sb + Au, Au + As, Pb + Zn + Ag, and Sb + Pb + Zn + Ag were selected to calculate their threshold values. The element association scores were calculated by first rescaling the element concentrations divided by their median value, in order to avoid creation of false anomalies due to different dimensions between or among the different elements, and thereafter performing addition. The anomaly threshold values calculated using different methods are shown in Table 3.

The threshold values for each element parameter are greater for the log-transformed data than for the raw data in each method category (Table 3). The C–A fractal model of these element concentrations, together with the scores of element associations, indicates that three line segments are fitted. These are termed low anomaly, high anomaly, and background (Fig. 7). The threshold values of the variables determined from the high anomaly of the C–A fractal model are so large that the anomalies show poor spatial association with known deposits in the North Himalaya (Table 3).

7. Discussion

The North Himalaya contains 10 Au deposits, 15 Sb deposits, 3 Sb–Pb–Zn–Ag deposits, and 1 Pb–Zn deposit, the distributions of which are used to evaluate the significance of the anomalies determined by different statistical methods (Fig. 8). The low anomaly threshold of 4.1 ppb for Au determined by C–A model delineates anomalies that show spatial associations with known mineralization in the North Himalaya, including 10 Au deposits, 9 Sb deposits, and 1 Sb–Pb–Zn–Ag deposits (Table 4). The Mean + 2STD raw data threshold value of 4.5 ppb delineates anomalous areas that are spatially associated with 9 Au deposits, 9 Sb deposits, and 2 Sb–Pb–Zn–Ag deposits (Table 4). Similarly, the Median + 2MAD with a threshold value of 5.0 ppb delineates anomalous areas that are spatially associated with 9 Au deposits and 2 Sb–Pb–Zn–Ag deposits, but only 5 Sb deposits (Table 4). The Mean + 2STD and Median + 2MAD log-transformed threshold values of 7.2 ppb and 6.0 ppb, respectively, are so high that only 6 Au deposits occur in the anomalous areas (Table 4). These results show that although the Au threshold generated using the C–A fractal model is the lowest, the anomalies produce the best spatial association to known Au, Sb, and Sb–Pb–Zn–Ag deposits in the North Himalaya.

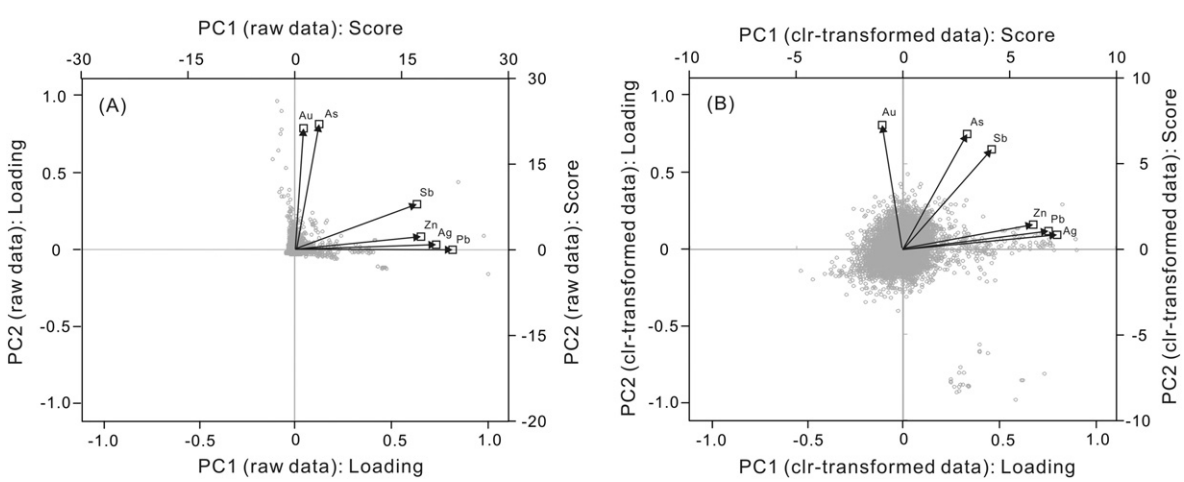

Fig. 6. Biplots of principal components obtained by raw data (A) and clr-transformed data (B).

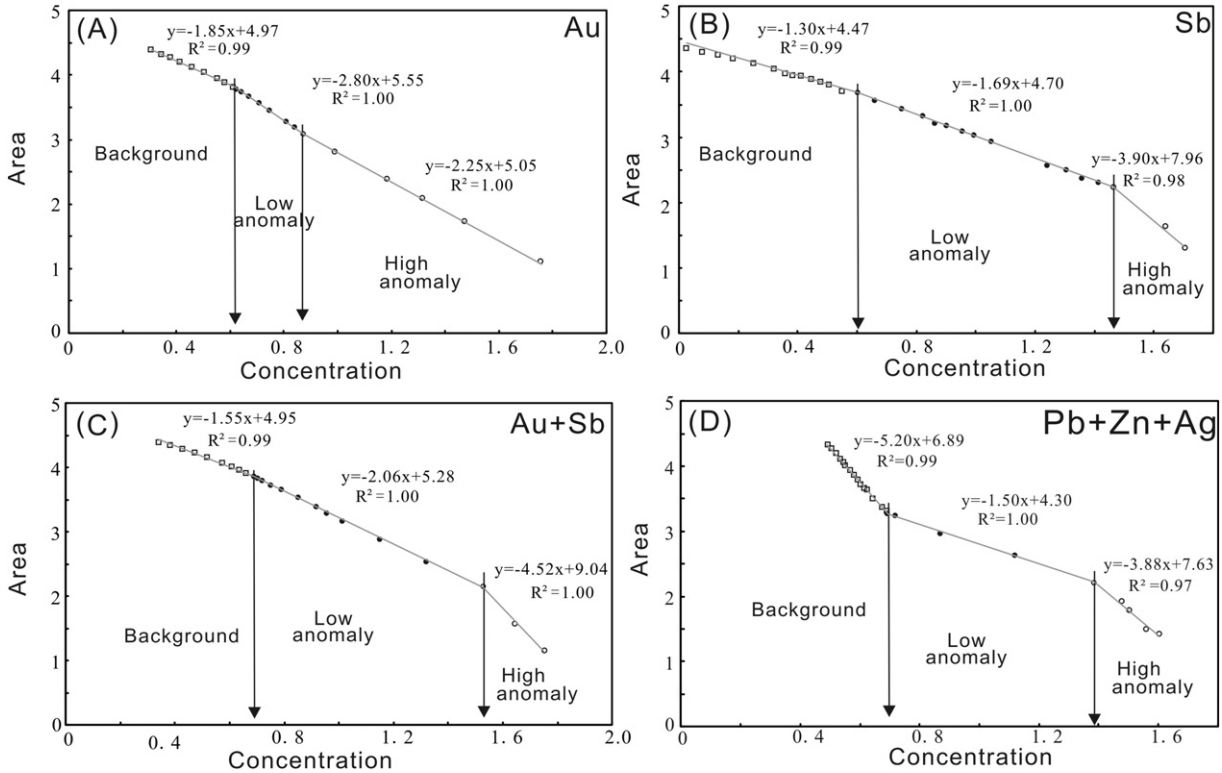

Fig. 7. Log–log (base e) plots showing the relationship between area and (A) Au, (B) Sb, (C) Sb + Au, and (D) Pb + Zn + Ag, generated using the C–A fractal model. Three straight-line segments are fitted by the least squares method.

For Au + As, the threshold values determined by the Mean + 2STD raw data, Median + 2MAD raw data, and C–A fractal model are better than those determined by other methods because the delineated anomaly areas contain the larger number of known Au deposits (8; Table 4). However, the Au anomaly areas determined by the same methods contain the largest number of known Au deposits (over 9; Table 4), which indicates that Au anomaly is more suitable for delineating Au mineralization than Au + As anomaly. It should be noted that Au + As association is shown in PC obtained by raw data whereas Au is shown in PC obtained by clr-transformed data. This also confirms that the PCA of clr-transformed data has priority over the classic PCA of raw data.

For Sb, all three methods generate threshold values that define anomalies spatially associated with the same number of known deposits in the North Himalaya (i.e., 12 Sb deposits, 3 Sb–Au deposits, and 3 Sb–Pb–Zn–Ag deposits) (Tables 3 and 4). Of these, the log-transformed Mean + 2STD method generates the highest Sb threshold value of 6.4 ppm, which corresponds to the lowest anomaly area (4.1% of the total area) and, consequently, the best spatial associations to known Sb deposits (Table 4). It should be noted that Sb anomalies determined by any methods show no spatial association with known Au deposits. This characteristic could be used for targeting Au deposits in the North Himalaya.

The threshold values of Sb + Au determined by these methods delineate anomalous areas that contain different numbers of Au deposits, but the same number of Sb, Sb–Au and Sb–Pb–Zn–Ag deposits. Of the known deposits associated with Sb, Sb–Au and Sb–Pb–Zn–Ag mineralization in the North Himalaya, the best spatial association is found using the Mean + 2STD log-transformed data for Sb + Au, which produces the highest threshold value and the smallest anomaly area (Table 4). In addition, both Sb + Au and Sb anomalies determined by Mean + 2STD for log-transformed data show spatial associations with the same deposits. Even so, the area of Sb + Au anomalies (which accounts for 3.6% of the total area) is smaller than the area of Sb anomalies (4.1% of the total area), indicating that Sb + Au anomalies are more effective than Sb alone when targeting Sb, Sb–Au, and Sb–Pb–Zn–Ag deposits. If we consider the association of Sb + Au anomalies with all known deposits in the North Himalaya, the C–A fractal model includes a larger number of deposits than the Mean + 2STD of log-transformed data. The total area of the Sb + Au anomalies determined by the low anomaly C–A fractal model is 13.2%. This exhibits spatial associations with seven known Au deposits, which is more than the number determined by the other methods (Table 4). However, Au anomalies identified using this method account for 11.9% of the total area and show spatial associations with 10 known Au deposits (Table 4). Therefore, we suggest that Au anomaly is more suitable for targeting Au deposits than Sb + Au anomaly.

All these methods produce Pb + Zn + Ag anomalies that show spatial associations with the same number of Pb–Zn and Sb–Pb–Zn–Ag deposits (1 and 3, respectively) in the North Himalaya. One exception is the Median + 2MAD of log-transformed data, which failed to predict a Pb–Zn deposit. Among these, the highest threshold value was generated by the C–A fractal model, which therefore produces the smallest anomaly area. Consequently, these results show that Pb + Zn + Ag anomalies estimated by the C–A fractal model are suitable for targeting Pb–Zn(−Ag) deposits in the North Himalaya.

Anomalies of Sb + Pb + Zn + Ag determined by Mean + 2STD for raw and log-transformed data, and by Median + 2MAD for raw data, exhibit spatial associations with the same Sb, Sb–Au and Sb–Pb–Zn–Ag deposits. Among the methods investigated, the Mean + 2STD for log-transformed data is the best at delineating anomalies in Sb + Pb + Zn + Ag, as this method generated the highest threshold value and, the lowest anomaly area (Tables 3 and 4).

Although anomalies in Sb or Sb + Au determined by all of the methods used in this study show spatial associations with 12 Sb deposits in the North Himalaya, these do not include the Baijia, Rila and Xiangdala Sb deposits. Considering that the local singularity method is highly effective at identifying weak geochemical anomalies, we applied this method to the geochemical stream sediment data, specifically for Sb. The window–based method was used to calculate the singularity index based on the total amount model using five square windows of

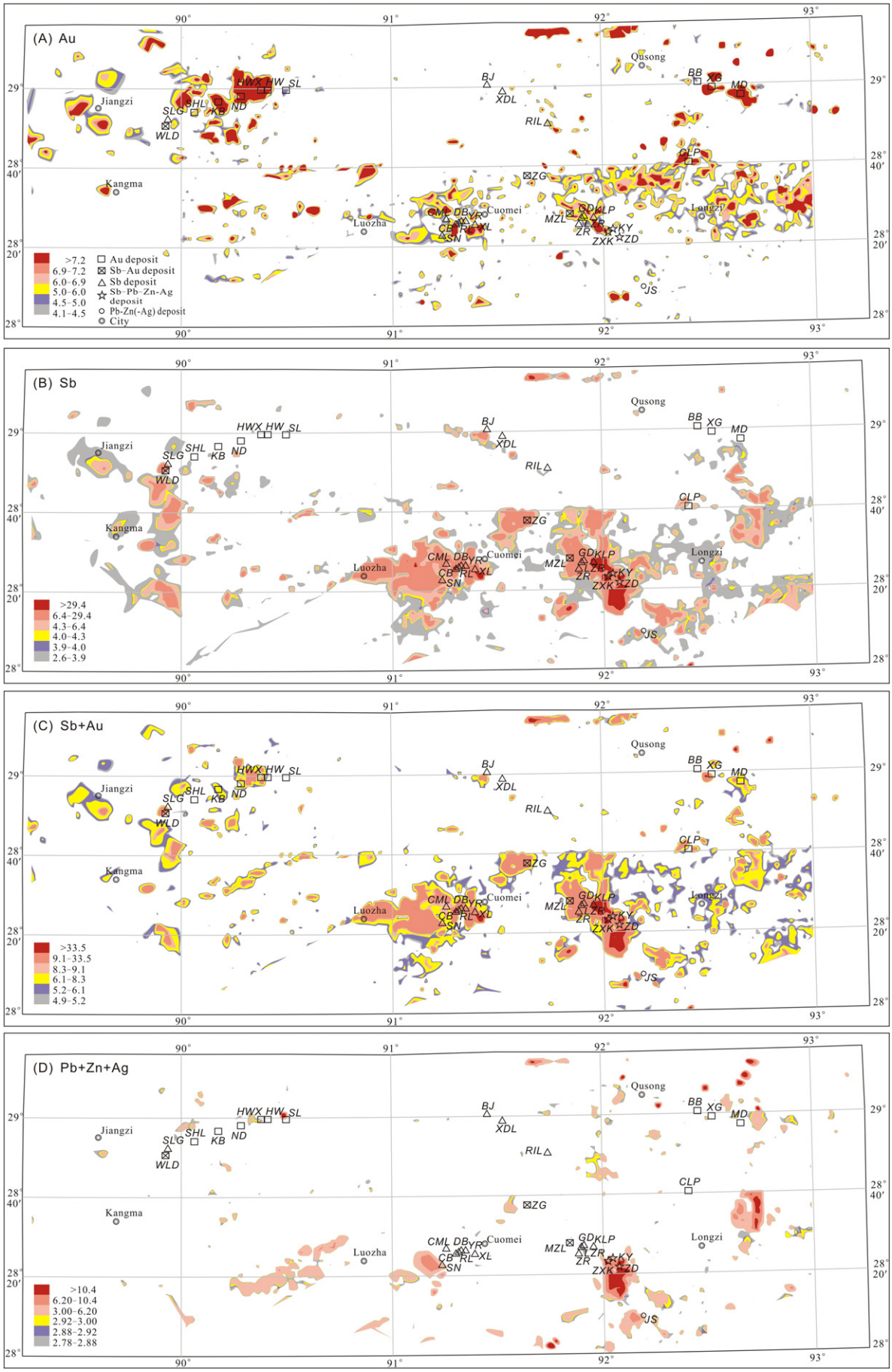

Fig. 8. Spatial distributions of anomalies of (A) Au, (B) Sb, (C) Sb + Au, and (D) Pb + Zn + Ag. Threshold values determined by different methods (Table 3) were used to define the intervals.

Table 4
Anomaly areas determined by different methods and their spatial associations with known deposits in the North Himalaya.

Anomalous areas	Mean + 2STD				Median + 2MAD				C-A fractal model			
	Raw data		log-transformed data		Raw data		log-transformed data		Low anomaly		High anomaly	
	I	II	I	II	I	II	I	II	I	II	I	II
Au	9.6%	Au(9), Sb(9) SbPbZnAg(2)	2.5%	Au(6)	7.4%	Au(9), Sb(5) SbPbZnAg(2)	4.4%	Au(6), Sb(2)	11.9%	Au(10), Sb(9) SbPbZnAg(2)	2.8%	Au(6) SbPbZnAg(2)
Sb	16.2%	Sb(12) SbAu(3) SbPbZnAg(3)	4.1%	Sb(12) SbAu(3) SbPbZnAg(3)	8.6%	Sb(12) SbAu(3) SbPbZnAg(3)	7.4%	Sb(12) SbAu(3) SbPbZnAg(3)	8.2%	Sb(12) SbAu(3) SbPbZnAg(3)	0.3%	Sb(2)
Sb + Au	11.8%	Au(6), Sb(12) AuSb(3) SbPbZnAg(3)	3.6%	Sb(12) AuSb(3) SbPbZnAg(3)	8.4%	Au(4), Sb(12) AuSb(3) SbPbZnAg(3)	6.5%	Au(4), Sb(12) AuSb(3) SbPbZnAg(3)	13.2%	Au(7), Sb(12) AuSb(3) SbPbZnAg(3)	0.3%	Sb(2) SbPbZnAg(2)
Au + As	8.2%	Au(8), Sb(8) AuSb(1) SbPbZnAg(2)	2.4%	Au(6), Sb(1) SbPbZnAg(2)	7.4%	Au(8), Sb(6) AuSb(1) SbPbZnAg(2)	4.8%	Au(6), Sb(3) SbPbZnAg(2)	15%	Au(8), Sb(11) AuSb(1), SbPbZnAg(3)	3.8%	Au(6), Sb(3) SbPbZnAg(2)
Pb + Zn + Ag	5.8%	PbZn (1) SbPbZnAg(3)	4.3%	PbZn (1) SbPbZnAg(3)	3.7%	PbZn (1) SbPbZnAg(3)	1.6%	SbPbZnAg(3)	3.2%	PbZn (1) SbPbZnAg(3)	0.3%	SbPbZnAg(2)
Sb + Pb + Zn + Ag	11.1%	Sb(12) PbZn(1) AuSb(3) SbPbZnAg(3)	6.8%	Sb(12) PbZn(1) AuSb(3) SbPbZnAg(3)	7.0%	Sb(12) PbZn(1) AuSb(3) SbPbZnAg(3)	7.8%	Sb(12) PbZn(1) AuSb(3) SbPbZnAg(3)	3.2%	Sb(10) AuSb(3) SbPbZnAg(3)	0.3%	Sb(1) SbPbZnAg(1)

Note: 'I' denotes the percentage of the total area delineated as anomalies. 'II' indicates the number of known deposits present within the anomalous areas (shown in brackets). The numbers of known deposits in the study area are as follows: 10 Au deposits, 15 Sb deposits, 3 Sb–Pb–Zn–Ag deposits, and 1 Pb–Zn deposit.

1.5 × 1.5, 4.5 × 4.5, 7.5 × 7.5, 10.5 × 10.5, and 13.5 × 13.5 km. Values of singularity (α) and squared correlation coefficient for Sb are shown in Fig. 9A and 9B. The squared correlation coefficients for Sb that are greater than 0.9 account for 80% of the total data, which indicates the existence of power-law relationships that satisfies Eq. (2) above. The threshold values were determined using the C–A fractal method (Fig. 9C) and were used to define the intervals and to map the distributions of the singularity (Fig. 9D). Anomalies in α–Sb determined using the high anomaly C–A fractal model ($\alpha = 1.47$) exhibit spatial associations with six Sb deposits (including the Baijia) in anomalous areas that accounts for 3.2% of the total area (Fig. 9D). If anomalies in α–Sb are determined by the low anomaly C–A model ($\alpha = 1.91$), the anomalous

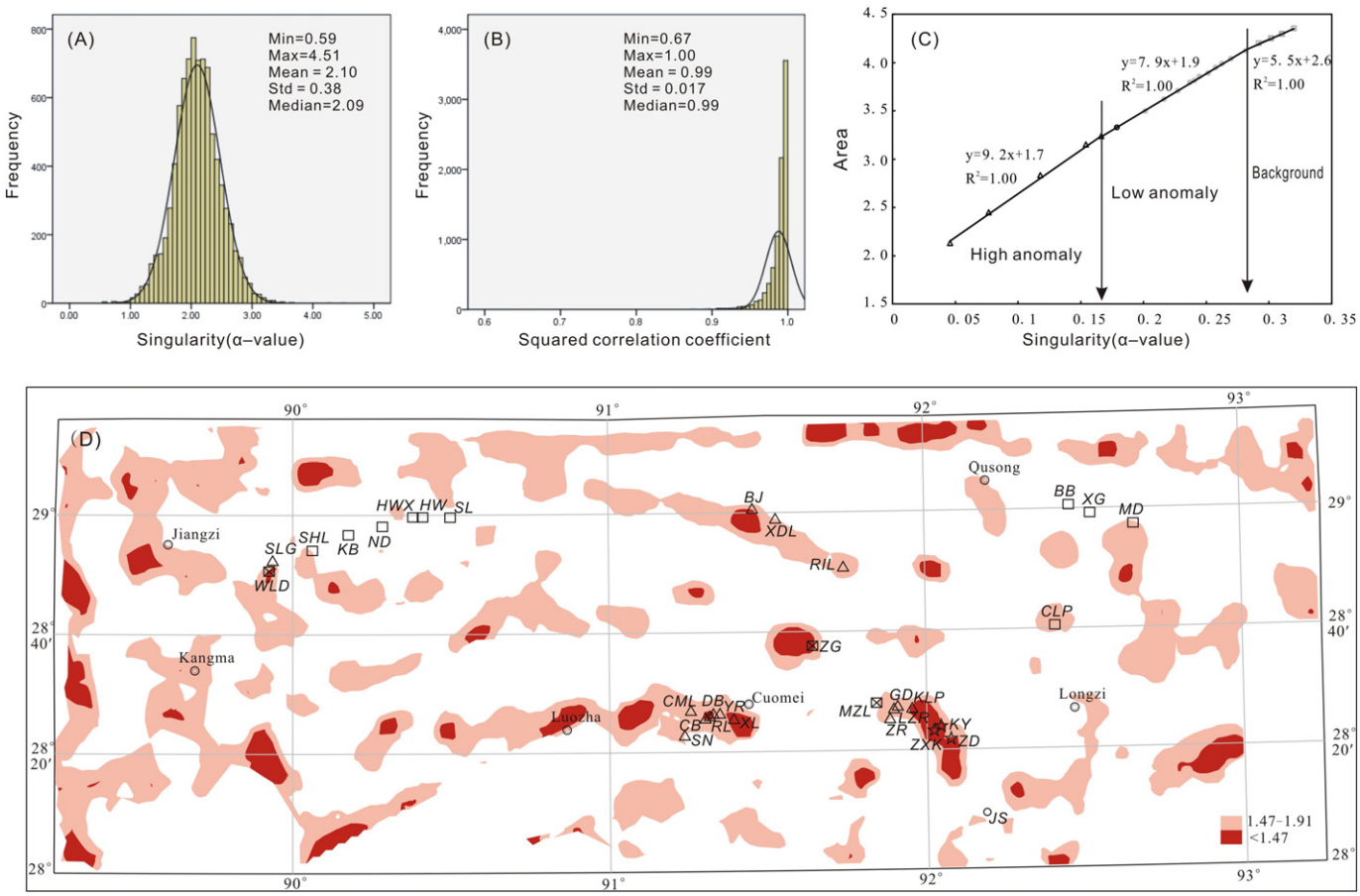

Fig. 9. (A) Histogram of α-values of Sb, (B) Histogram of squared correlation coefficients of Sb. (C) Log–log (base 10) plot showing the relationship between area A(≥C) and the Sb singularity value (C) using the C–A fractal model. Three straight-line segments are fitted using the least squares method, and two break points separating line segments are taken as the threshold values. (D) Spatial distribution of the Sb singularity value. The threshold values shown in Fig. 9C were used to define the intervals.

areas accounts for 24% of the total area and contains 12 Sb deposits (including the Baijia, Rila, and Xiangdala). These results suggest that the singularity method can identify weak anomalies associated with Sb mineralization at Baijia, Rila, and Xiangdala. However, the singularity method did not identify anomalies associated with the other three Sb deposits, whose anomalies can be delineated by Mean + 2STD for log-transformed data. In addition, these results show that values of α–Sb < 2 occupy almost 40% of the total data, and that in many cases the areas with anomalies in α–Sb differ from the areas with anomalies in Sb or Sb + Au. These results suggest that the singularity method should be combined with other methods to identify geochemical anomalies.

8. Conclusions

(1) The geochemical data should be processed for reducing the effect of data closure problem. PCA of clr-transformed stream sediment geochemical data in the North Himalaya can accurately recognize three types of mineralization, i.e. Au, Pb–Zn–Ag and Sb. Anomalies of Au shown in PC of clr-transformed data show better spatial association with known deposits than those of Au + As shown in PC of raw data. In addition, PCs of raw data only show Sb–Pb–Zn–Ag assemblage, whereas those of clr-transformed data show Pb–Zn–Ag and Sb–As assemblages.

(2) Both the C–A fractal model and Mean + 2STD for log-transformed data are able to identify the geochemical anomalies associated with known mineralization in the North Himalaya. Prior to applying the method of Mean + 2STD, we should reject those extreme values through multiple iterations until the remaining data follow the normal distribution.

(3) Anomalies of Au are more suitable for targeting Au mineralization than those of Au + As and Sb + Au. The best method for delineating Au anomaly is the C–A fractal model. Sb anomalies show no spatial association with Au deposits. The best approach for targeting Sb deposits is to use Sb anomaly determined by the Mean + 2STD of log-transformed data and that for targeting both Sb and Sb–Au deposits is to use Sb + Au anomaly determined by the Mean + 2STD of log-transformed data. The best approaches for targeting Pb–Zn(−Ag) and Sb–Pb–Zn–Ag deposits is to employ Pb + Zn + Ag anomaly determined by the C–A fractal model, and Sb + Pb + Zn + Ag anomaly determined by the Mean + 2STD for log-transformed data, respectively.

(4) The local singularity method can identify weak anomalies associated with Sb mineralization and should be combined with other methods to identify geochemical anomalies in the North Himalaya.

Conflict of interest

We declare that we do not have any commercial or associative interest that represents a conflict of interest in connection with the work submitted.

Acknowledgments

We thank Dr. Franco Pirajno and two anonymous reviewers for their insightful comments. This research was supported by the National Key Project for Basic Research of China (2011CB403106, 2015CB452600), Changjiang Scholars and Innovative Research Team in University (IRT14R54, IRT1083), Program of the China Geological Survey (1212011220664), Fundamental Research Funds for the Central Universities, and Beijing Higher Education Young Elite Teacher Project.

References

Afzal, P., Alghalandis, Y.F., Khakzad, A., Moarefvand, P., Omran, N.R., 2011. Delineation of mineralization zones in porphyry Cu deposits by fractal concentration–volume modeling. J. Geochem. Explor. 108 (3), 220–232.
Agterberg, F., 1995. Multifractal modeling of the sizes and grades of giant and supergiant deposits. Int. Geol. Rev. 37 (1), 1–8.
Aikman, A.B., Harrison, T.M., Lin, D., 2008. Evidence for early (>44 Ma) Himalayan crustal thickening, Tethyan Himalaya, southeastern Tibet. Earth Planet. Sci. Lett. 274, 14–23.
Aikman, A.B., Harrison, T.M., Hermann, J., 2012. Age and thermal history of Eo- and Neohimalayan granitoids, eastern Himalaya. J. Asian Earth Sci. 51, 85–97.
Aitchison, J., 1986. The Statistical Analysis of Compositional Data. Chapman & Hall, London.
Armijo, R., Tapponnier, P., Mercier, J., Han, T.L., 1986. Quaternary extension in southern Tibet: field observations and tectonic implications. J. Geophys. Res. 91, 13803–13872.
Carranza, E.J.M., 2004. Usefulness of stream order to detect stream sediment geochemical anomalies. Geochem. Explor. Environ. Anal. 4 (4), 341–352.
Carranza, E.J.M., 2010. Mapping of anomalies in continuous and discrete fields of stream sediment geochemical landscapes. Geochem. Explor. Environ. Anal. 10 (2), 171–187.
Cheng, Q., 2007. Mapping singularities with stream sediment geochemical data for prediction of undiscovered mineral deposits in Gejiu, Yunnan Province, China. Ore Geol. Rev. 32 (1), 314–324.
Cheng, Q., Agterberg, F., Ballantyne, S., 1994. The separation of geochemical anomalies from background by fractal methods. J. Geochem. Explor. 51 (2), 109–130.
Cheng, Q., Jing, L., Panahi, A., 2006. Principal component analysis with optimum order sample correlation coefficient for image enhancement. Int. J. Remote Sens 16, 3387–3401.
Cheng, Q., Xu, Y., Grunsky, E., 2000. Multifractal power spectrum-area method for geochemical anomaly separation. Nat. Resour. Res. 9, 43–51.
Cheng, Q., Bonham-Carter, G., Wang, W., Zhang, S., Li, W., Qinglin, X., 2011. A spatially weighted principal component analysis for multi-element geochemical data for mapping locations of felsic intrusions in the Gejiu mineral district of Yunnan, China. Comput. Geosci. 37 (5), 662–669.
Deng, J., Wang, Q.F., Wan, L., Yang, L.Q., Gong, Q.J., Zhao, J., Liu, H., 2009. Self-similar fractal analysis of gold mineralization of Dayingezhuang disseminated-veinlet deposit in jiaodong gold province, China. J. Geochem. Explor. 102 (2), 95–102.
Deng, J., Wang, Q.F., Yang, L.Q., Wang, Y.R., Gong, Q.J., Liu, H., 2010. Delineation and explanation of geochemical anomalies using fractal models in the Heqing area, Yunnan Province, China. J. Geochem. Explor. 105 (3), 95–105.
Deng, J., Wang, Q.F., Wan, L., Liu, H., Yang, L.Q., Zhang, J., 2011. A multifractal analysis of mineralization characteristics of the Dayingezhuang disseminated-veinlet gold deposit in the Jiaodong gold province of China. Ore Geol. Rev. 40 (1), 54–64.
Deng, J., Wang, Q.F., Li, G.J., Santosh, M., 2014a. Cenozoic tectono-magmatic and metallogenic processes in the Sanjiang region, southwestern China. Earth Sci. Rev. 138, 268–299.
Deng, J., Wang, Q.F., Li, G.J., Li, C.S., Wang, C.M., 2014b. Tethys tectonic evolution and its bearing on the distribution of important mineral deposits in the Sanjiang region, SW China. Gondwana Res. 26, 419–437.
Deng, J., Wang, Q.F., Li, G.J., Zhao, Y., 2015. Structural control and genesis of the Oligocene Zhenyuan orogenic gold deposit, SW China. Ore Geol. Rev. 65, 42–54.
Egozcue, J.J., Pawlowsky-Glahn, V., Mateu-Figueras, G., Barcelo-Vidal, C., 2003. Isometric logratio transformations for compositional data analysis. Math. Geol. 35 (3), 279–300.
HMCL, 2012. Ore Resource Report of the Zhaxikang Sb–Pb–Zn–Ag Deposit, Southern Tibet (Internal Report). Huayu Mining Corporation Limited, Tibet (in Chinese).
Hou, Z.Q., Cook, N.J., 2009. Metallogenesis of the Tibetan collisional orogen: a review and introduction to the special issue. Ore Geol. Rev. 36, 2–24.
Hou, Z.Q., Zheng, Y.C., Zeng, L.S., Gao, L.E., Huang, K.X., Li, W., Li, Q.Y., Fu, Q., Liang, W., Sun, Q.Z., 2012. Eocene–Oligocene granitoids in southern Tibet: constraints on crustal anatexis and tectonic evolution of the Himalayan orogen. Earth Planet. Sci. Lett 349, 38–52.
Ji, W.Q., Wu, F.Y., Liu, C.Z., Chung, S.L., 2009. Geochronology and petrogenesis of granitic rocks in Gangdese batholith, Southern Tibet. Sci. China Ser. D Earth Sci. 52, 1240–1261.
Kaiser, H.F., 1960. The application of electronic computers to factor analysis. Educ. Psychol. Meas. 20, 141–151.
Li, C., Ma, T., Shi, J., 2003. Application of a fractal method relating concentrations and distances for separation of geochemical anomalies from background. J. Geochem. Explor. 77 (2), 167–175.
Liang, W., Hou, Z., Yang, Z., Li, Z., Huang, K., Zhang, S., Li, W., Zheng, Y., 2013. Remobilization and overprinting in the Zhaxikang Pb–Zn–Ag–Sb polymetal ore deposit, Southern Tibet: implications for its metallogenesis. Acta Petrol. Sin. 29 (11), 3828–3842 (In Chinese with English abstract).
Lin, B., Tang, J.X., Zheng, W.B., Leng, Q.F., Yang, C., Tang, X.Q., Hang, Y., Wang, Y.Y., Tan, J.Y., 2014. Petrochemical features, zircon U-Pb dating and Hf isotopic composition of the rhyolite in Zhaxikang deposit, Southern Xizang (Tibet). Geol. Rev. 60, 178–189 (In Chinese with English abstract).
Liu, G., Einsele, G., 1994. Sedimentary history of the tethyan basin in the Tibetan Himalayas. Geol. Rundsch. 82, 32–61.
Mandelbrot, B.B., 1983. The fractal geometry of nature. Freeman, San Francisco, p. 468.
Pan, G., Ding, J., Yao, D., 2004. Geological map of Qinghai–Xizang (Tibet) Plateau and Adjacent Areas (1:1500000): Chengdu Institute of Geology and Mineral Resources, China Geological Survey. Chengdu Cartographic Publishing House, Chengdu.
Reimann, C., Filzmoser, P., Garrett, R.G., 2005. Background and threshold: critical comparison of methods of determination. Sci. Total Environ. 346 (1), 1–16.
Reimann, C., Filzmoser, P., Garrett, R.G., Dutter, R., 2008. Statistical Data Analysis Explained: Applied Environmental Statistics with R. Wiley, Chichester, UK, p. 362.

Sinclair, A., 1974. Selection of threshold values in geochemical data using probability graphs. J. Geochem. Explor. 3 (2), 129–149.
Sun, X., Deng, J., Gong, Q., Wang, Q., Yang, L., Zhao, Z., 2009. Kohonen neural network and factor analysis based approach to geochemical data pattern recognition. J. Geochem. Explor. 103 (1), 6–16.
Sun, X., Gong, Q., Wang, Q., Yang, L., Wang, C., Wang, Z., 2010a. Application of local singularity model to delineate geochemical anomalies in Xiong'ershan gold and molybdenum ore district, Western Henan province, China. J. Geochem. Explor. 107 (1), 21–29.
Sun, X., Wei, H., Zhai, W., Shi, G., Lian, Y., Mo, R., Han, M., Yi, J., 2010b. Ore-forming fluid geochemistry and metallogenic mechanism of Bangbu large-scale orogenic gold deposit in southern Tibet, China. Acta Petrol. Sin. 26 (6), 1672–1684 (In Chinese with English abstract).
Taylor, M., Yin, A., Ryerson, F.J., Kapp, P., Ding, L., 2003. Conjugate strike–slip faulting along the Bangong–Nujiang suture zone accommodates coeval east–west extension and north–south shortening in the interior of the Tibetan Plateau. Tectonics 22. http://dx.doi.org/10.1029/(2002)TC001361.
Tukey, J.W., 1977. Exploratory data analysis. Addison-Wesley, Reading 7.
Wang, Q.F., Deng, J., Liu, H., Yang, L.Q., Wan, L., Zhang, R.Z., 2010a. Fractal models for ore reserve estimation. Ore Geol. Rev. 37, 2–14.
Wang, Q.F., Deng, J., Zhao, J., Liu, H.A., Wan, L., Yang, L.Q., 2010b. Tonnage-cutoff model and average grade-cutoff model for a single ore deposit. Ore Geol. Rev. 38, 113–120.
Wang, Q.F., Deng, J., Liu, H., Wang, Y., Sun, X., Wan, L., 2011a. Fractal models for estimating local reserves with different mineralization qualities and spatial variations. J. Geochem. Explor. 108, 196–208.
Wang, X., Xie, X., Zhang, B., Hou, Q., 2011b. Geochemical probe into China's continental crust. Acta Geosci. Sin. 32, 65–83 (In Chinese with English abstract).
Wang, Q.F., Deng, J., Zhao, J., Li, N., Wan, L., 2012. The fractal relationship between orebody tonnage and thickness. J. Geochem. Explor. 122, 4–8.
Wu, F.Y., Ji, W.Q., Wang, J.G., Liu, C.Z., Chung, S.L., Cliet, P.D., 2014. Zircon U–Pb and Hf isotopic constraints on the onset time of India–Asia collision. Am. J. Sci. 314, 548–579.
Xie, X., Mu, X., Ren, T., 1997. Geochemical mapping in China. J. Geochem. Explor. 60 (1), 99–113.
Xie, X., Wang, X., Zhang, Q., Zhou, G., Cheng, H., Liu, D., Cheng, Z., Xu, S., 2008. Multi-scale geochemical mapping in China. Geochem. Explor. Environ. Anal. 8 (3–4), 333–341.
Yang, L.Q., Wang, Q.F., Liu, X.F., 2015. Correlation between mineralization intensity and fluid-rock reaction in the Xinli gold deposit, Jiaodong Peninsula, China: constraints from petrographic and statistical approaches. Ore Geol. Rev. 71, 29–39.
Yin, A., 2006. Cenozoic tectonic evolution of the Himalayan orogen as constrained by along-strike variation of structural geometry, exhumation history, and foreland sedimentation. Earth Sci. Rev. 76 (1), 1–131.
Zeng, L., Gao, L., Xie, K., Jing, L., 2011. Mid-Eocene high Sr/Y granites in the northern Himalayan gneiss domes: melting thickened lower continental crust. Earth Planet. Sci. Lett. 303 (3), 251–266.
Zhai, W., Sun, X., Yi, J., Zhang, X., Mo, R., Zhou, F., Wei, H., Zeng, Q., 2014. Geology, geochemistry, and genesis of orogenic gold–antimony mineralization in the Himalayan Orogen, South Tibet, China. Ore Geol. Rev. 58, 68–90.
Zhang, J., Santosh, M., Wang, X., Guo, L., Yang, X., Zhang, B., 2012. Tectonics of the northern Himalaya since the India–Asia collision. Gondwana Res. 21 (4), 939–960.
Zheng, Y., Liu, M., Sun, X., Yuan, E., Tian, L., Zheng, H., Zhang, G., Zhang, L., 2012. Type, discovery process and significance of Zhaxikang antimony polymetallic ore deposit, Tibet. Earth Science—Journal of China University of. Geosciences 37, 1003–1014 (In Chinese with English abstract).
Zheng, Y., Sun, X., Gao, S., Wang, C., Zhao, Z., Wu, S., Li, J., Wu, X., 2014a. Analysis of stream sediment data for exploring the Zhunuo porphyry Cu deposit, southern Tibet. J. Geochem. Explor. 143, 19–30.
Zheng, Y., Sun, X., Tian, L., Zheng, H., Yu, M., Yang, W., Zhou, T., Geng, X., 2014b. Mineralization, deposit type and metallogenic age of the gold antimony polymetallic belt in the eastern part of North Himalayan. Geotecton. Metallog. 38 (1), 108–118 (In Chinese with English abstract).
Zhu, D.C., Mo, X.X., Pan, G.T., Zhao, Z.D., Dong, G.C., Shi, Y.R., Liao, Z.L., Wang, L.Q., Zhou, C.Y., 2008. Petrogenesis of the earliest Early Cretaceous mafic rocks from the cona area of the eastern Tethyan Himalaya in south Tibet: interaction between the incubating Kerguelen plume and the eastern Greater India lithosphere. Lithos 100, 147–173.
Zhu, D.C., Chung, S.L., Mo, X.X., Zhao, Z.D., Niu, Y.L., Song, B., Yang, Y.H., 2009. The 132 Ma Comei-Bunbury large igneous province: remnants identified in present-day southeastern Tibet and southwestern Australia. Geology 37, 583–586.
Zhu, D.C., Zhao, Z.D., Niu, Y.L., Mo, X.X., Chung, S.L., Hou, Z.Q., Wang, L.Q., Wu, F.Y., 2011. The Lhasa terrane, record of a microcontinent and its histories of drift and growth. Earth Planet. Sci. Lett. 301, 241–255.
Zuo, R., 2014. Identification of geochemical anomalies associated with mineralization in the Fanshan district, Fujian, China. J. Geochem. Explor. 139, 170–176.
Zuo, R., Cheng, Q., Agterberg, F., Xia, Q., 2009. Application of singularity mapping technique to identify local anomalies using stream sediment geochemical data, a case study from Gangdese, Tibet, western China. J. Geochem. Explor. 101 (3), 225–235.
Zuo, R., Xia, Q., Zhang, D., 2013. A comparison study of the C–A and S–A models with singularity analysis to identify geochemical anomalies in covered areas. Appl. Geochem. 33, 165–172.